Shiva-DiT: Residual-Based Differentiable Top-k Selection for Efficient Diffusion Transformers

Jiaji Zhang [1]   **Hailiang Zhao** [1]   **Guoxuan Zhu** [2]   **Ruichao Sun** [1]   **Jiaju Wu** [3]   **Xinkui Zhao** [1]   **Hanlin Tang** [2]
Weiyi Lu [2]   **Kan Liu** [2]   **Tao Lan** [2]   **Lin Qu** [2]   **Shuiguang Deng** [1]

Abstract

Diffusion Transformers (DiTs) incur prohibitive computational costs due to the quadratic scaling of self-attention. Existing pruning methods fail to simultaneously satisfy differentiability, efficiency, and the strict static budgets required for hardware overhead. To address this, we propose *Shiva-DiT*, which effectively reconciles these conflicting requirements via *Residual-Based Differentiable Top-k Selection*. By leveraging a residual-aware straight-through estimator, our method enforces deterministic token counts for static compilation while preserving end-to-end learnability through residual gradient estimation. Furthermore, we introduce a Context-Aware Router and Adaptive Ratio Policy to autonomously learn an adaptive pruning schedule. Experiments on mainstream models, including SD3.5, demonstrate that Shiva-DiT establishes a new Pareto frontier, achieving a $1.54\times$ wall-clock speedup with superior fidelity compared to existing baselines, effectively eliminating ragged tensor overheads.

1. Introduction

The advent of Diffusion Transformers (DiTs) marks a paradigm shift in generative modeling (Peebles & Xie, 2023; Chen et al., 2025; Esser et al., 2024; Black Forest Labs, 2024). By scaling standard architectures, DiTs are transcending visual fidelity to emerge as general-purpose world simulators that model physical dynamics (Brooks et al., 2024; Gemini Team, Google, 2025). However, this performance comes at a prohibitive computational cost. Unlike U-Nets (Ronneberger et al., 2015), which operate on compressed feature maps, DiTs process flattened sequences of spatial tokens, where the self-attention mechanism scales

quadratically with resolution. For a standard 1024×1024 image, processing 4096 tokens per layer across dozens of timesteps creates a massive latency bottleneck, hindering real-time deployment.

To mitigate this, dynamic token pruning has emerged as a critical direction. However, designing an efficient pruning mechanism for DiTs requires balancing three conflicting objectives, which we term the *Trilemma of Sparse Learning* (see Figure 1a): **1) Differentiability**, to ensure the policy is end-to-end learnable for capturing complex diffusion semantics; **2) Efficiency**, requiring minimal training overhead to ensure scalability on high-resolution inputs; and **3) Strict Budget**, enforcing a deterministic top-k count to guarantee static tensor shapes. This final constraint is essential for hardware-friendly static compilation (e.g., CUDA Graphs) and efficient `gather`/`scatter` primitives, effectively avoiding the latency overhead of ragged tensors.

Existing approaches typically compromise on at least one of these vertices. Heuristic methods (Bolya & Hoffman, 2023; Wu et al., 2025; Lu et al., 2025; Fang et al., 2025) ensure hardware compatibility but lack learnability, relying on static rules that fail to capture semantic nuances. Conversely, learnable masking methods inspired by Gumbel-Softmax (Zhao et al., 2025) achieve differentiability but treat pruning as a thresholding problem. This results in *ragged tensors* with variable sequence lengths, which preclude the use of static graph compilation and introduce significant kernel launch overheads. While DiffCR (You et al., 2025) attempts to bridge this gap by learning a fixed budget via interpolation, it incurs prohibitive training overhead, necessitating dual forward passes to estimate gradients, which effectively doubles the training cost. Similarly, soft-ranking operators like NeuralSort (Grover et al., 2019) offer differentiable top-k, but constructing the required $N \times N$ permutation matrix during training incurs a quadratic memory footprint, rendering them intractable for high-resolution vision tasks.

In this paper, we introduce *Shiva-DiT*, a framework that resolves the efficiency-quality trilemma via *Residual-Based Differentiable Sorting*. By leveraging the backbone's residual nature, we formulate a gradient estimator that models

(a) The Trilemma of Sparse Learning.
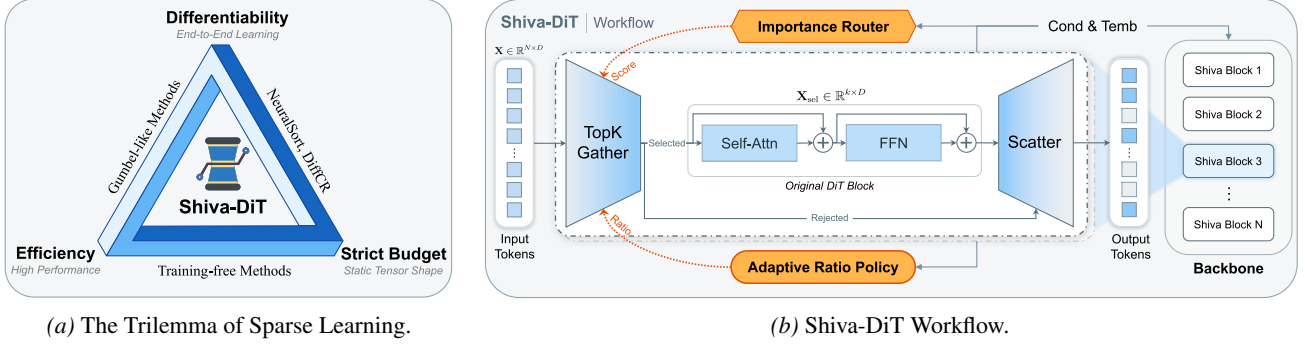
(b) Shiva-DiT Workflow.

Figure 1. **Overview of Shiva-DiT.** (a) Shiva simultaneously resolves the sparse learning trilemma: Differentiability, Efficiency, and Strict Budget. (b) We inject a lightweight *Importance Router* and *Adaptive Ratio Policy* into the frozen backbone. Utilizing differentiable sorting, Shiva ensures learnability while maintaining static tensor shapes for hardware efficiency.

pruning as a learnable selection between the active block and the identity skip connection. This design enables the end-to-end optimization of a deterministic token budget k, enforcing hardware-friendly static tensor shapes. To fully exploit this, we incorporate a *Context-Aware Router* using a pairwise layer-sharing strategy and an *Adaptive Ratio Policy* that learns a decoupled spatiotemporal schedule, thereby automatically allocating computation to information-dense generative stages without manual heuristics.

Our contributions are summarized as follows: (1) We propose a *Residual-Based Differentiable Sorting* mechanism that formulates token pruning as a differentiable top-k selection within residual blocks. By deriving a novel gradient estimator, this design enables the end-to-end optimization of a learnable budget k, providing the mathematical foundation for adaptive pruning while maintaining a hardware-friendly deterministic execution flow. (2) We introduce a *Context-Aware Router* and an *Adaptive Ratio Policy* to achieve intelligent computation allocation. This architecture autonomously learns a spatiotemporally adaptive pruning schedule by capturing local feature consistency and global diffusion dynamics, eliminating the reliance on manual heuristics. (3) Extensive experiments on mainstream DiT models, including SD3.5, demonstrate that Shiva-DiT establishes a new Pareto frontier. Our method achieves a $1.54\times$ wall-clock speedup while maintaining superior generative fidelity compared to state-of-the-art baselines (Zhao et al., 2025; Wu et al., 2025).

2. Related Work

2.1. Token Reduction in Vision Transformers

The imperative to mitigate the quadratic complexity of self-attention originated in discriminative Vision Transformers (ViTs) (Dosovitskiy et al., 2021). Pioneering works (Rao et al., 2021; Marin et al., 2023; Bolya et al., 2023; Zhang et al., 2024b; Wang et al., 2024a; Lee et al., 2024) explored

various strategies such as dynamic pruning, token pooling, and bipartite matching to eliminate redundant tokens. Notably, Token Fusion (Kim et al., 2024) bridges the gap between pruning and merging, selecting operations based on functional linearity and introducing MLERP to preserve feature norms. While these methods established the groundwork for efficiency, their design assumptions do not fully align with the generative nature of DiTs (Peebles & Xie, 2023). However, these methods are tailored for classification, where discarding background is harmless. In contrast, diffusion models require dense prediction for pixel-level generation. Therefore, applying aggressive pruning naively to DiTs compromises spatial integrity and image fidelity.

2.2. Heuristic and Training-Free Acceleration

To adapt reduction techniques to diffusion, ToMeSD (Bolya & Hoffman, 2023) extended token merging to Stable Diffusion, introducing unmerge operations to preserve spatial consistency. To better preserve semantic details, subsequent works incorporated advanced saliency metrics. AT-EDM (Wang et al., 2024b) evaluates token importance using attention maps, while IBTM (Wu et al., 2025) leverages classifier-free guidance (CFG) scores to protect high-information tokens. Other approaches explore spectral or optimization perspectives: FreqTS (Yang et al., 2025) prioritizes high-frequency components encoding structural details, and ToMA (Lu et al., 2025) reformulates token selection as a submodular optimization problem. Leveraging the temporal dynamics, SDTM (Fang et al., 2025) utilizes the "structure-then-detail" denoising prior, applying a hand-crafted schedule to merge tokens aggressively in early structural stages. While effective as post-training optimizations, such heuristic policies are inherently static and may not optimally adapt to complex redundancy patterns.

Kernel Incompatibility. A practical bottleneck for methods relying on explicit attention maps (e.g., ranking via QK^T (Wang et al., 2024b;a; Fang et al., 2025)) is their

conflict with hardware-efficient attention algorithms. State-of-the-art implementations like FlashAttention (Dao et al., 2022) employ tiling-based parallel algorithms that compute attention scores block-by-block in fast on-chip SRAM. Crucially, these algorithms *never materialize* the complete $N \times N$ attention map in High-Bandwidth Memory (HBM). Pruning algorithms that mandate access to the global attention map inevitably force a fallback to quadratic-memory implementations, thereby negating the scalability and speed benefits of modern attention kernels.

2.3. Temporal Feature Caching

Accelerating inference by exploiting feature correlation between adjacent timesteps has also gained traction. DiT-FastAttn (Yuan et al., 2024) identifies redundancies across spatial and temporal dimensions, proposing cross-timestep attention sharing. ToCa (Zou et al., 2025) and DaTo (Zhang et al., 2024a) introduce token-wise caching based on dynamics, updating only critical tokens while reusing cached features for others. Similarly, CA-ToMe (Saghatchian et al., 2025) and AsymRnR (Sun et al., 2025) extend merging results across steps. While effective for standard sampling regimes, these strategies fundamentally rely on the assumption of *temporal continuity*. This dependency may limit their applicability in accelerated inference scenarios, such as few-step distillation, where the feature distribution evolves rapidly between discrete timesteps. By avoiding reliance on historical feature alignment, our approach maintains a generalized design suitable for diverse sampling schedules.

2.4. Learning-Based Dynamic Architectures

To surpass heuristic limitations, recent research focuses on learning-based dynamic pruning. DyDiT (Zhao et al., 2025) trains lightweight routers but relies on threshold-based masking, leading to unpredictable computational budgets. SparseDiT (Chang et al., 2025) re-architects DiT with sparse modules, though it requires invasive modifications. Addressing ratio learning, DiffCR (You et al., 2025) proposes timestep-adaptive ratios via linear interpolation. However, this approach necessitates computationally expensive dual forward passes for differentiable ratio. In contrast, Shiva-DiT integrates pruning decisions directly into a single pass, reducing training cost by $\sim$35% compared to consistency-based baselines, as detailed in Appendix B.4. By employing a fully differentiable top-k mechanism, our framework ensures a *deterministic* budget and provides *fine-grained* token gradients without the overhead or architectural invasiveness of prior arts.

3. Method

3.1. Preliminaries

Unified Perspective on Generative Models. We unify Denoising Diffusion Probabilistic Models (DDPMs) (Ho et al., 2020) and Flow Matching frameworks (Lipman et al., 2023) under a common objective: learning a time-dependent backbone $F_\theta(\mathbf{x}_t, t, c)$ to minimize the regression error

$$\mathcal{L} = \mathbb{E}_{t, \mathbf{x}_0, \mathbf{x}_1} \left[\|F_\theta(\mathbf{x}_t, t, c) - \mathbf{y}_t\|^2 \right]. \tag{1}$$

Here, the regression target $\mathbf{y}_t$ varies by architecture, representing either the noise ϵ in legacy models (e.g., SD1.5 (Rombach et al., 2022), SDXL (Podell et al., 2024)) or the velocity field v_t in modern flow matching approaches (e.g., Flux (Black Forest Labs, 2024), SD3 (Esser et al., 2024)). Since *Shiva-DiT* optimizes the internal token processing efficiency of F_θ, it is fundamentally agnostic to the specific prediction target (noise vs. velocity) and compatible with off-the-shelf samplers (e.g., DDIM (Song et al., 2021), Euler (Karras et al., 2022) and DPM (Lu et al., 2022)).

Backbone Architecture. We focus on models where the backbone F_θ is instantiated as a Diffusion Transformer (DiT) (Peebles & Xie, 2023). The input latent is flattened into a sequence of N spatial tokens $\mathbf{X} \in \mathbb{R}^{N \times D}$, where D is the hidden dimension. These tokens are processed by L transformer layers. A generic block at layer ℓ updates the sequence via:

$$\begin{aligned} \mathbf{Y}_\ell &= \mathbf{X}_\ell + \text{Attention}(\text{Norm}(\mathbf{X}_\ell, c, t)), \\ \mathbf{X}_{\ell+1} &= \mathbf{Y}_\ell + \text{FFN}(\text{Norm}(\mathbf{Y}_\ell, c, t)). \end{aligned} \tag{2}$$

Problem Formulation. Regardless of the prediction target, the computational bottleneck lies in the sequence length N, as Attention (Vaswani et al., 2017) scales with $\mathcal{O}(N^2)$ and FFN with $\mathcal{O}(N)$. Our goal is to introduce a differentiable selection mechanism within these blocks to dynamically identify a sparse subset $\mathbf{X}_{\text{sel}} \in \mathbb{R}^{k \times D}$ ($k \ll N$) for computation, thereby accelerating the entire iterative generation process.

3.2. Residual-Based Differentiable Sorting

To overcome the non-differentiability of top-k selection without the overhead of soft masking (Jang et al., 2017) or the coarseness of binning (You et al., 2025), we propose *Residual-Based Differentiable Sorting*. This mechanism enables efficient hard selection during inference while maintaining accurate gradient estimation for both token scores and the budget k during training.

Forward Pass: Hard Selection. To strictly enforce computational acceleration, the forward pass executes a deterministic hard selection. Let $\mathbf{X} \in \mathbb{R}^{N \times D}$ denote the input

tokens and $\mathbf{s} \in \mathbb{R}^N$ be the corresponding importance scores predicted by the Router. Given a target budget k, we identify the index set of the top-k scores:

$$\mathcal{I}_{\text{topk}} = \text{argtopk}(\mathbf{s}, k). \tag{3}$$

The token set is physically partitioned into selected ($\mathbf{X}_{\text{sel}}$) and rejected ($\mathbf{X}_{\text{rej}}$) subsets via a gather operation:

$$\mathbf{X}_{\text{sel}} = \{\mathbf{x}_i \mid i \in \mathcal{I}_{\text{topk}}\}, \quad \mathbf{X}_{\text{rej}} = \mathbf{X} \setminus \mathbf{X}_{\text{sel}}. \tag{4}$$

Crucially, subsequent Transformer layers process only $\mathbf{X}_{\text{sel}}$, reducing FLOPs strictly proportional to the reduction ratio.

Backward Pass: Gradient Estimation. Since the discrete indicator function $\mathbb{I}(i \in \mathcal{I}_{\text{topk}})$ has zero gradients, we construct a differentiable surrogate graph. Inspired by stochastic relaxation (Burges et al., 2005), we inject Gaussian noise $\epsilon \sim \mathcal{N}(0, \sigma^2)$ into the scores ($\tilde{\mathbf{s}} = \mathbf{s} + \epsilon$) and compute a *descending soft rank* $\tilde{r}_i$ via pairwise sigmoid comparisons (detailed in Algorithm 1):

$$\tilde{r}_i(\tilde{\mathbf{s}}) = 1 + \sum_{j \neq i} \sigma\left(\frac{\tilde{s}_j - \tilde{s}_i}{\tau_{\text{rank}}}\right), \tag{5}$$

where τ_{rank} is the temperature. Crucially, while Eq. (5) entails $O(N^2)$ comparisons, this operation is restricted *exclusively* to the scalar scores $\tilde{\mathbf{s}} \in \mathbb{R}^{N \times 1}$. This explicitly avoids the prohibitive $O(N^2 D)$ overhead of feature-wise soft-sorting methods like NeuralSort (Grover et al., 2019), ensuring the memory footprint remains negligible compared to the backbone's attention maps.

To enable gradient flow to the learnable budget k, we formulate the inclusion score π_i as a continuous relaxation (Jang et al., 2017) of the binary selection indicator:

$$\pi_i(\tilde{\mathbf{s}}, k) = \sigma\left(\frac{k - \tilde{r}_i(\tilde{\mathbf{s}})}{\tau_{\text{sel}}}\right), \tag{6}$$

where τ_{sel} is a temperature parameter. This formulation creates a fully differentiable path: $\frac{\partial \pi_i}{\partial \mathbf{s}}$ and $\frac{\partial \pi_i}{\partial k}$ are nonzero. Note that in this relaxed view, k acts as a continuous threshold against the soft ranks.

Residual-Based Gradient Estimator. To propagate gradients through the non-differentiable bottleneck, we employ a *Residual-Based Straight-Through Estimator* (STE). Since the deterministic hard selection restricts observation to a single path per token, we define the gradient of the selection probability π_i based on the feature sensitivity of the actually executed path. A detailed discussion on this estimator and its gradient formulation is provided in Appendix A.2.

$$\frac{\partial \mathcal{L}}{\partial \pi_i} \approx \begin{cases} \langle \nabla_{\mathbf{x}_i}^{\text{sel}} \mathcal{L}, \ \mathbf{x}_i \rangle & \text{if } i \in \mathcal{I}_{\text{topk}} \\ -\langle \nabla_{\mathbf{x}_i}^{\text{rej}} \mathcal{L}, \ \mathbf{x}_i \rangle & \text{if } i \notin \mathcal{I}_{\text{topk}} \end{cases}, \tag{7}$$

Algorithm 1 Differentiable Soft Rank Calculation

1: **Input:** Perturbed Scores $\tilde{\mathbf{S}} \in \mathbb{R}^{B \times N}$, Temp τ
2: **Output:** Soft Ranks $\mathbf{R} \in \mathbb{R}^{B \times N}$
3: $\mathbf{D} \leftarrow (\tilde{\mathbf{S}}_{:,1,:} - \tilde{\mathbf{S}}_{:,:,1})/\tau$ $\quad \triangleright$ Broadcast differences
4: $\mathbf{P} \leftarrow \sigma(\mathbf{D}) \cdot (1 - \mathbf{I})$ $\quad \triangleright$ Exclude self-comparison
5: $\mathbf{R} \leftarrow 1 + \sum_k \mathbf{P}_{:,:,k}$ $\quad \triangleright$ Sum over the last dimension
6: **return** $\mathbf{R}$

---

where ∇^{sel} and ∇^{rej} denote the gradients of the loss $\mathcal{L}$ with respect to the effective input features under the selected and rejected paths, respectively. In practice, this piecewise formulation is implemented efficiently via vectorized tensor operations, where the negative sign for rejected tokens acts as a corrective signal to penalize erroneous routing decisions.

Comparison with Existing Paradigms. Our mechanism addresses critical limitations in prior arts. First, regarding *Budget Controllability*, Gumbel-based methods (Jang et al., 2017) like DyDiT (Zhao et al., 2025) rely on prediction-then-threshold masking. This paradigm suffers from budget instability and results in ragged tensors that are incompatible with efficient batching or gather operations. In contrast, our explicit top-k selection decouples budgeting from ranking, guaranteeing exact adherence to budget k and enabling efficient, hardware-friendly inference with regular tensors. Second, regarding *Gradient Granularity*, interpolation-based methods like DiffCR (You et al., 2025) necessitate expensive dual forward passes and derive coarse gradients solely from bin slopes. Conversely, our differentiable sorting enables efficient *single-pass* estimation with *fine-grained* visibility into individual token contributions via Eq. 6, allowing for end-to-end optimization without computational redundancy.

3.3. Context-Aware Token Importance Router

Token importance in diffusion is inherently contextual: a spatial token's redundancy depends on the denoising stage, its semantic alignment with the text prompt, and its abstraction level within the network. Unlike prior heuristics that rely on local metrics like L2 norms or attention scores, we propose the *ShivaRouter*. This lightweight, context-conditioned scoring network efficiently captures these multi-dimensional dependencies to predict token informativeness.

Architecture. To efficiently capture multi-dimensional dependencies, the router predicts a scalar importance score s_i by conditioning the local token feature $\mathbf{x}_i \in \mathbb{R}^D$ on three global signals: global semantics $\mathbf{c}$ and temporal embedding t (both reused from the pre-trained backbone), alongside a learnable layer identity embedding l. We project these inputs into a low-dimensional bottleneck space ($d' = 64$)

and apply an additive fusion to minimize overhead:

$$\mathbf{h}_{\text{ctx}} = \text{Proj}_t(t) + \text{Proj}_p(\mathbf{c}) + \text{Proj}_l(l), \qquad (8)$$

$$s_i = \mathbf{w}^{\text{T}} \cdot \text{LayerNorm}\left(\sigma(\text{Proj}_x(\mathbf{x}_i) + \mathbf{h}_{\text{ctx}})\right), \quad (9)$$

where Proj_* denote lightweight linear projections and σ is the SiLU activation. This design acts as a conditional shift, modulating the token's latent representation based on context. The layer embedding l is particularly crucial, as it allows the router to distinguish nuances between specific layers within a shared parameter group.

Locally Shared Parameters. To balance representation capacity with parameter efficiency, we evaluate different router sharing configurations across network depths. While independent routers for each layer maximize flexibility, our empirical results show that *Pairwise Sharing* (grouping every two adjacent layers to share one router) provides the optimal trade-off. This strategy effectively captures the local feature consistency between consecutive blocks while significantly reducing parameter overhead. Experiments confirm that this localized sharing maintains generative quality more effectively than either layer-specific or globally-shared routers.

3.4. Adaptive Ratio Policy

Determining optimal pruning ratios across layers and timesteps is challenging. Prior methods often rely on static heuristics (Chang et al., 2025) or discrete timestep buckets (You et al., 2025), failing to capture the fine-grained dynamics of the diffusion process. To address this, we introduce a *Ratio Policy Network*, a lightweight controller that predicts a continuous, context-aware retention ratio $r_{t,l} \in (0, 1]$. This ratio determines the discrete budget $k = \lfloor N \cdot r_{t,l} \rfloor$ (as discussed in Sec. 3.2), enabling precise and continuous control over hardware-constrained token counts throughout the generation.

Continuous Decoupled Modulation. We hypothesize that the optimal sparsity profile can be decomposed into a superposition of a static spatial prior and a global temporal trend. Unlike multiplicative mechanisms such as FiLM (Perez et al., 2018), which inherently assume that temporal dynamics exert complex, layer-specific scaling effects (i.e., different timesteps modulate different layers non-uniformly), we argue that the redundancy trend across timesteps is largely consistent across network depths. Therefore, we adopt a *Decoupled Additive* architecture to explicitly treat spatial and temporal redundancies as independent, additive factors.

Let $\mathbf{e}_\ell \in \mathbb{R}^d$ be a learnable embedding for layer ℓ, and $\mathbf{e}_t = \text{MLP}(t)$ be the projected timestep embedding. The

policy predicts the logit of the retention ratio via:

$$\text{logit}(r_{t,\ell}) = \Phi_{\text{time}}(\mathbf{e}_t) + \Phi_{\text{layer}}(\mathbf{e}_\ell) + b_{\text{anchor}}, \qquad (10)$$

$$r_{t,\ell} = \sigma(\text{logit}(r_{t,\ell})), \qquad (11)$$

where Φ denotes lightweight MLPs and b_{anchor} is a learnable scalar initialized to $\sigma^{-1}(R_{\text{target}})$. This additive design not only stabilizes optimization but also guarantees inference efficiency. Crucially, since the policy network Φ depends solely on the timestep t and layer index ℓ, and is independent of dynamic input tokens or text prompts, the predicted ratios are deterministic for a given checkpoint. Consequently, during inference, the entire policy network is compiled into a lightweight *Look-Up Table* (LUT), introducing negligible computational overhead to the generation process.

Stabilized Budget Constraint. Optimizing a dynamic policy to satisfy a global budget R_{target} involves a trade-off between stability and flexibility. Prior methods like DyDiT (Zhao et al., 2025) produce unpredictable costs via thresholding, while DiffCR (You et al., 2025) penalizes mini-batch deviations from the target ($\|\bar{r}_{\text{batch}} - R_{\text{target}}\|^2$). While effective for spatially static policies, this rigid constraint is ill-suited for time-dependent pruning schedules. By forcing every mini-batch to strictly adhere to the target, it precludes the flexibility required to allocate varying computational budgets across different diffusion timesteps.

To support time-dependent pruning, we introduce an *Exponential Moving Average (EMA)* μ_{global} to decouple the budget constraint from the sparse mini-batch sampling. At iteration k, it tracks the long-term retention ratio via:

$$\mu_{\text{global}}^{(k)} = \beta \cdot \bar{r}_{\text{batch}}^{(k)} + (1 - \beta) \cdot \mu_{\text{global}}^{(k-1)}, \qquad (12)$$

where $\bar{r}_{\text{batch}}$ is the globally synchronized batch mean. We then formulate a proxy linear budget loss:

$$\mathcal{L}_{\text{budget}} = \lambda \cdot \bar{r}_{\text{batch}} \cdot \text{sg}\left[2 \cdot (\mu_{\text{global}} - R_{\text{target}})\right], \qquad (13)$$

where $\text{sg}[\cdot]$ denotes the stop-gradient operator, and μ_{global} utilizes the updated moving average (from Eq. 12) to strictly enforce the budget constraint based on the latest global statistics. This formulation constructs a dynamic gradient field: the term in brackets acts as a directional signal, pushing $\bar{r}_{\text{batch}}$ downwards only when the global average exceeds the budget (and vice versa). This anchors the global constraint while allowing the policy to explore optimal spatiotemporal allocations. The stability of this mechanism is further ensured by *Stratified Timestep Sampling* (Sec. 3.5), which minimizes the variance of $\bar{r}_{\text{batch}}$ and provides a stable signal for the EMA.

3.5. Training Objectives and Strategy

To effectively optimize the router's discrete decisions and the policy's continuous constraints alongside the backbone,

| Vanilla | ToMeSD | IBTM | DiffCR | DyDiT | **Shiva-DiT** | *Finetuned* |

Figure 2. Qualitative Comparison. Prompt: *God Zeus wearing a golden oak leaves crown on his head, grey beard.* By directing token reduction to the background, Shiva-DiT preserves high-fidelity subject details (e.g., beard, weaving) comparable to Vanilla, whereas competitors degrade the primary figure.

we employ a composite objective function and a multi-stage training process.

Composite Loss with Distillation. The total objective integrates diffusion reconstruction $\mathcal{L}_{\text{diff}}$, budget constraint $\mathcal{L}_{\text{budget}}$, and distillation terms:

$$\mathcal{L}_{\text{total}} = \mathcal{L}_{\text{diff}} + \lambda_b \mathcal{L}_{\text{budget}} + \lambda_d \mathcal{L}_{\text{distill}}. \tag{14}$$

To ensure semantic consistency, we incorporate multi-scale distillation from the frozen teacher model. Specifically, we apply feature alignment losses every 4 transformer blocks (Zhao et al., 2025) alongside a final output distillation loss, defined as Normalized Feature Distillation (see Eq. (31) in Appendix B.2), providing dense supervision to guide the router's optimization.

Staged Training Protocol. Directly optimizing all components from a cold start can lead to instability. We therefore adopt a progressive three-stage strategy, consisting of *Router Warmup*, *Policy Learning*, and *Joint Tuning*, to sequentially establish ranking capability, optimize the budget schedule, and recover generation fidelity. Detailed configurations for each stage are provided in Appendix B.2.

Stratified Sampling Strategy. To stabilize the joint optimization of the modules, we introduce a *Stratified Sampling* mechanism to rectify the high variance of standard uniform sampling.

1) Stratified Timestep Sampling. Standard sampling $t \sim \mathcal{U}(0, T)$ often leads to temporal clustering within a mini-batch, destabilizing the budget controller. We instead enforce uniform coverage by partitioning the domain $[0, T]$ into B equi-width intervals for a global batch size B, drawing one sample t_i from each:

$$t_i \sim \mathcal{U}\left(\frac{i \cdot T}{B}, \frac{(i+1) \cdot T}{B}\right), \quad i \in \{0, \ldots, B-1\}. \tag{15}$$

As detailed in Appendix A.4, this ensures $\bar{r}_{\text{batch}}$ acts as a low-variance estimator of the global expectation, providing a stable gradient signal for optimization.

2) Stratified Ratio Sampling. Primarily utilized during the router warmup stage, this strategy forces the router to learn a robust global ranking capability across the full sparsity spectrum before the policy network is activated. Specifically, we partition the batch into K groups, assigning each a target r_k sampled from disjoint intervals spanning $[r_{\min}, r_{\max}]$. This prevents the router from overfitting to local decision boundaries at fixed ratios, ensuring compatibility with the subsequent dynamic schedule.

4. Experiments

4.1. Main Results

Experimental Settings. We evaluate Shiva-DiT on SD3.5-Medium (Esser et al., 2024), Flux.1-dev (Black Forest Labs, 2024), and PixArt-Σ (Chen et al., 2025) using PEFT (Mangrulkar et al., 2022) on the MJHQ-30K (Li et al., 2024) dataset. Training is conducted on $8\times$ NVIDIA H200 GPUs (30–50 hours), while inference metrics are measured on an NVIDIA RTX 4090. We compare against two categories of baselines: (1) **Training-free methods**, including ToMeSD (Bolya & Hoffman, 2023), ToFu (Kim et al., 2024), SDTM (Fang et al., 2025), ToMA (Lu et al., 2025) and IBTM (Wu et al., 2025); (2) **Training-based methods**, including SparseDiT (Chang et al., 2025), DiffCR (You et al., 2025) and DyDiT (Zhao et al., 2025). Note that we exclude NeuralSort (Grover et al., 2019) because it requires explicit multiplication with an $N \times N$ permutation matrix, incurring a computational complexity of $\mathcal{O}(N^2 D)$ and prohibitive memory costs. This heavy overhead effectively negates the potential speedup from token reduction, making it unsuitable for our acceleration target.

For fairness, all training-based baselines are re-implemented within our unified framework using the same dataset. Crucially, we utilize their official training objectives and configurations (e.g., distillation for DyDiT (Zhao et al., 2025), standard MSE for DiffCR (You et al., 2025)) to ensure their optimal performance, while Shiva-DiT follows the proposed staged protocol. Detailed configurations and generalization results on Flux.1-dev (Black Forest Labs, 2024) and PixArt-Σ (Chen et al., 2025) are provided in Appendix B.2 and B.6.

Table 1. Quantitative results on SD3.5 (1024×1024, 50 steps, measured on RTX 4090). Metrics include IR (ImageReward), CLIP (CLIP Score), and IQA (CLIP-IQA). *Finetuned* denotes the LoRA-based model serving as the quality upper bound (sharing the same inference cost as *Vanilla*). Our methods achieve the superior trade-off between efficiency and fidelity.

Methods	Image Quality Metrics				Efficiency Metrics			
	FID ↓	IR ↑	CLIP ↑	IQA ↑	FLOPs (T)	Latency (ms)	Speedup	Δ FLOPs (%)
Vanilla	16.86	0.9385	30.89	0.4567	11.80	7659.9	1.00×	0.0
Finetuned	*13.22*	*1.0179*	*31.18*	*0.4743*				
ToMeSD (2023)	40.22	0.6727	30.88	0.4632	8.98	7352.9	1.04×	23.9
ToFu (2024)	47.43	0.4157	30.36	0.4655	8.98	7296.7	1.05×	23.9
SDTM (2025)	47.08	0.3257	29.96	0.4705	8.83	7180.6	1.07×	25.2
ToMA (2025)	30.06	0.7033	30.83	0.4633	<u>8.23</u>	7406.5	1.03×	<u>30.3</u>
IBTM (2025)	19.96	0.8610	30.88	0.4695	10.18	7526.6	1.02×	13.7
DiffCR (2025)	17.51	0.7884	30.81	0.4941	9.93	6709.8	1.14×	15.8
DyDiT (2025)	<u>15.29</u>	0.7844	30.65	0.4824	9.42	6553.9	1.17×	20.2
SparseDiT (2025)	25.71	0.7751	30.56	0.4795	8.95	6211.3	1.24×	24.2
Shiva-80%	**13.83**	<u>0.8915</u>	<u>31.10</u>	**0.5051**	8.92	<u>6112.6</u>	<u>1.25×</u>	24.4
Shiva-60%	16.42	**0.9974**	**31.35**	<u>0.4952</u>	**6.96**	**4989.0**	**1.54×**	**41.0**

Main Results on SD3.5. Table 1 and Figure 2 demonstrate Shiva-DiT's superior trade-off between fidelity and latency. Specifically, Shiva-80% achieves the best FID (13.83) among all acceleration methods and the highest IQA (0.5051), effectively establishing a new Pareto frontier closely matching the finetuned upper bound. Notably, Shiva-60% secures a $1.54\times$ wall-clock speedup while maintaining a CLIP score (31.35) that surpasses even the finetuned baseline. We attribute this qualitative gain to the selective removal of redundant background tokens, which effectively acts as a spatial attention mechanism, forcing the model to allocate generation capacity to salient regions.
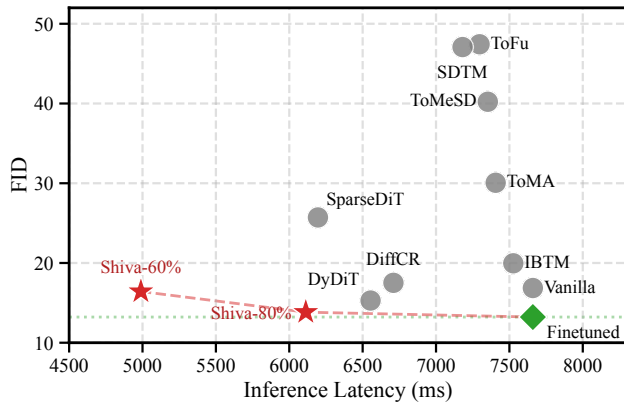

Figure 3. Efficiency-Quality Trade-off. Shiva-DiT pushes the Pareto frontier towards the bottom-left, achieving a superior balance between inference latency and FID compared to baselines.

Hardware-Aware Efficiency. We investigate the gap between theoretical FLOPs reduction and practical acceleration. As shown in Figure 3, optimization-heavy methods like ToMA (Lu et al., 2025) suffer from high runtime overhead due to iterative solving processes. Similarly, DyDiT (Zhao et al., 2025) relies on ragged tensors and online mask com-

putation, incurring significant memory re-allocation costs. In contrast, Shiva-DiT enforces strictly static tensor shapes, incurring negligible architectural overhead during the hard forward pass beyond a lightweight top-k selection. This design minimizes allocator churn and ensures seamless compatibility with static compilation pipelines (e.g., TensorRT).

Table 2. Router Configurations. We evaluate sharing strategies at a fixed 0.6 pruning ratio. Fidelity is measured via MSE (Mean Squared Error of reconstructed features) and Sim (Cosine Similarity between student and teacher features). *Group-12* achieves the best alignment, outperforming the unstable *Max* and layer-independent *Slim* baselines.

Config	Grouping	G	d'	Params	MSE ↓	Sim ↑
Tiny	Global	1	64	0.3M	2.102	0.829
Shared	Global	1	512	2.6M	1.254	0.862
Max	Independent	24	512	64M	1.831	0.805
Slim	Independent	24	64	8.0M	1.072	0.862
Group-4	6-Layers	4	128	2.7M	1.074	0.858
Group-8	3-Layers	8	64	2.7M	<u>0.906</u>	<u>0.879</u>
Group-12	Pairwise	12	64	4.1M	**0.894**	**0.881**

4.2. Ablation Study

Router Architecture Analysis. Table 2 examines the trade-off between parameter sharing and generalization. Global sharing ($G = 1$) yields suboptimal reconstruction, indicating that significant depth-wise feature heterogeneity precludes a single unified policy. Conversely, the independent baseline (Max) suffers from overfitting due to over-parameterization. By exploiting local feature consistency, our pairwise strategy achieves the lowest MSE (0.894). This adjacent-layer sharing acts as a regularizer, mitigating domain shifts while preserving discriminative power. Figure 5 confirms this qualitatively, showing accurate isolation of salient regions despite the reduced parameter count.
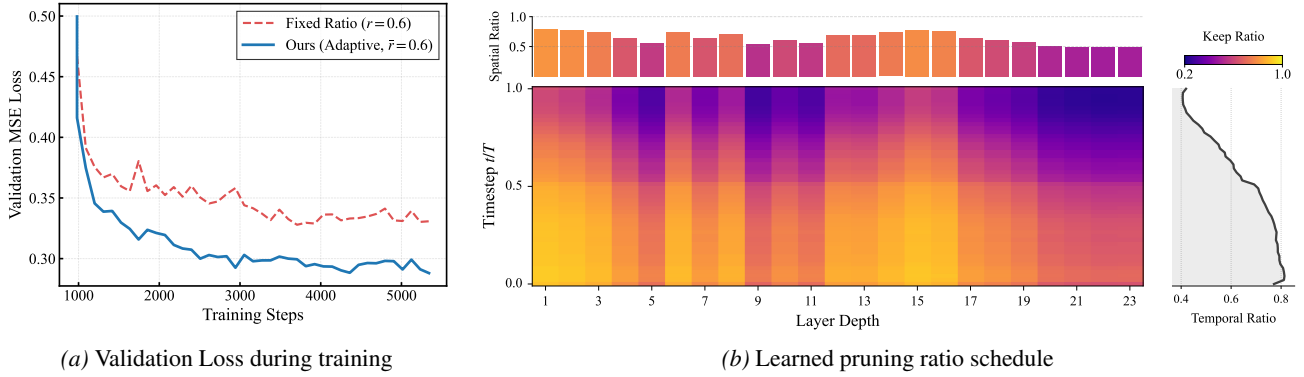
(a) Validation Loss during training

(b) Learned pruning ratio schedule

Figure 4. Adaptive Policy Analysis. (a) The adaptive policy achieves consistently lower validation MSE, indicating superior convergence. (b) The heatmap illustrates the pruning ratios across network layers (y-axis) and diffusion timesteps (x-axis), revealing a clear "structure-first, detail-later" preference.

Impact of Adaptive Ratio Policy. We evaluate our policy against a Fixed Ratio baseline under a strict budget ($\bar{r} \approx 0.6$). As shown in Figure 4(a) and Table 3, our adaptive approach achieves lower validation MSE and superior perceptual metrics by dynamically prioritizing information-dense regions. Visualizing the learned schedule (Figure 4) reveals a convergence to a *structure-first* spatial strategy (preserving shallow layers) and a progressive temporal pattern: distinct from the uniform baseline, it allocates maximum budget (≈ 0.8) to high-frequency refinement stages for detail recovery while aggressively pruning (≈ 0.4) during early chaotic structural phases.

Table 3. Ratio Policy Analysis on MJHQ-30K. We compare our Adaptive Policy with the Fixed baseline under an identical token budget ($\bar{r} \approx 0.6$) to ensure fair comparison.

Policy	FID ↓	ImageReward ↑	CLIP Score ↑	CLIP IQA ↑
Fixed Ratio	21.76	0.835	30.75	0.497
Adaptive	**17.36**	**0.880**	**30.94**	**0.500**

Analysis of Gradient Estimator and Budget Learning. We highlight that a standard Straight-Through Estimator (STE) is mathematically insufficient for our framework, as it cannot propagate gradients to the budget parameter k (since $\partial \mathbb{I}/\partial k = 0$ almost everywhere). Our Residual-Based Estimator (Eq. (7)) is specifically designed to bridge this gap. Therefore, the "Fixed Ratio" baseline (Table 3) effectively serves as the ablation study for our learnable budget mechanism: without our specific gradient estimator, the model effectively degenerates to a static pruning schedule. We further validate the directional correctness of our estimator via synthetic tasks in Appendix A.3, proving it successfully guides k to the optimal sparsity (Figure 6a).

Limitations. Shiva-DiT relies on the assumption of spatial redundancy, which weakens in high-density scenarios such as dense text rendering or crowded scenes. As our current implementation discards rejected tokens to strictly enforce
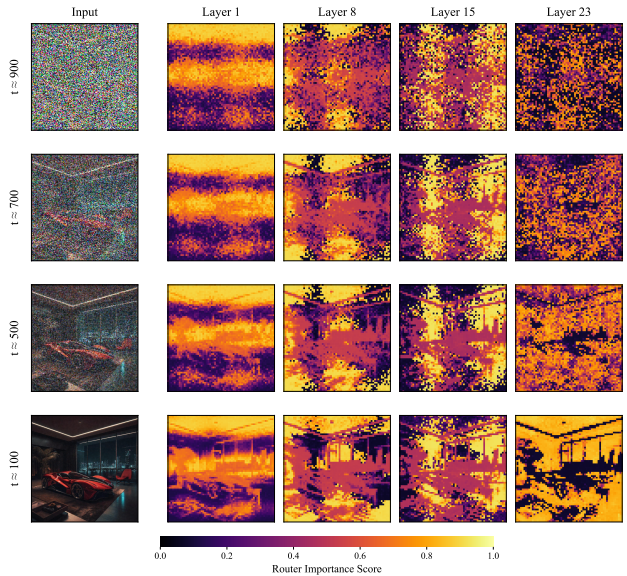

Figure 5. Visualization of Learned Masks (Group-12). The pairwise router effectively identifies semantic regions (e.g., foreground objects) and texture-rich areas, demonstrating that locally shared policies can accurately capture token importance.

the hardware budget, detail loss may occur when redundancy is minimal. Future work could investigate fusion strategies to aggregate information from rejected tokens into the active set, rather than discarding them entirely.

5. Conclusion

Shiva-DiT bridges the gap between theoretical FLOPs reduction and practical hardware acceleration. By reformulating token pruning as differentiable sorting within a residual framework, we enforce static tensor constraints without compromising generative capability. This work highlights the value of hardware-algorithm co-design, offering a scalable and efficient path for deploying large-scale diffusion backbones in real-time scenarios.

Impact Statement

This paper presents work whose goal is to advance the field of Machine Learning. There are many potential societal consequences of our work, none which we feel must be specifically highlighted here.

References

Black Forest Labs. Flux.1, 2024. URL https://blackforestlabs.ai/. Accessed: 2025-05-05.

Bolya, D. and Hoffman, J. Token merging for fast stable diffusion. *CVPR Workshop on Efficient Deep Learning for Computer Vision*, 2023.

Bolya, D., Fu, C.-Y., Dai, X., Zhang, P., Feichtenhofer, C., and Hoffman, J. Token merging: Your ViT but faster. In *International Conference on Learning Representations*, 2023.

Brooks, T., Peebles, B., Holmes, C., DePue, W., Guo, Y., Jing, L., Schnurr, D., Taylor, J., Luhman, T., Luhman, E., Ng, C., Wang, R., and Ramesh, A. Video generation models as world simulators. 2024. URL https://openai.com/research/video-generation-models-as-world-simulators.

Burges, C., Shaked, T., Renshaw, E., Lazier, A., Deeds, M., Hamilton, N., and Hullender, G. Learning to rank using gradient descent. In *Proceedings of the 22nd International Conference on Machine Learning*, ICML '05, pp. 89–96, New York, NY, USA, 2005. Association for Computing Machinery. ISBN 1595931805. doi: 10.1145/1102351.1102363. URL https://doi.org/10.1145/1102351.1102363.

Chang, S., WANG, P., Tang, J., Wang, F., and Yang, Y. Sparsedit: Token sparsification for efficient diffusion transformer. In *The Thirty-ninth Annual Conference on Neural Information Processing Systems*, 2025. URL https://openreview.net/forum?id=jTBxyQempF.

Chen, J., Ge, C., Xie, E., Wu, Y., Yao, L., Ren, X., Wang, Z., Luo, P., Lu, H., and Li, Z. Pixart-σ: Weak-to-strong training of diffusion transformer for 4k text-to-image generation. In Leonardis, A., Ricci, E., Roth, S., Russakovsky, O., Sattler, T., and Varol, G. (eds.), *Computer Vision – ECCV 2024*, pp. 74–91, Cham, 2025. Springer Nature Switzerland. ISBN 978-3-031-73411-3.

Dao, T., Fu, D. Y., Ermon, S., Rudra, A., and Ré, C. FlashAttention: Fast and memory-efficient exact attention with IO-awareness. In *Advances in Neural Information Processing Systems (NeurIPS)*, 2022.

Dosovitskiy, A., Beyer, L., Kolesnikov, A., Weissenborn, D., Zhai, X., Unterthiner, T., Dehghani, M., Minderer, M., Heigold, G., Gelly, S., Uszkoreit, J., and Houlsby, N. An image is worth 16x16 words: Transformers for image recognition at scale. *ICLR*, 2021.

Esser, P., Kulal, S., Blattmann, A., Entezari, R., Müller, J., Saini, H., Levi, Y., Lorenz, D., Sauer, A., Boesel, F., Podell, D., Dockhorn, T., English, Z., and Rombach, R. Scaling rectified flow transformers for high-resolution image synthesis. In *Proceedings of the 41st International Conference on Machine Learning*, ICML'24. JMLR.org, 2024.

Fang, H., Tang, S., Cao, J., Zhang, E., Tang, F., and Lee, T. Attend to not attended: Structure-then-detail token merging for post-training dit acceleration. In *IEEE/CVF Conference on Computer Vision and Pattern Recognition, CVPR 2025, Nashville, TN, USA, June 11-15, 2025*, pp. 18083–18092. Computer Vision Foundation / IEEE, 2025. doi: 10.1109/CVPR52734.2025.01685.

Gemini Team, Google. Gemini 3 technical report. Technical report, Google DeepMind, 2025. URL https://deepmind.google/technologies/gemini/.

Grover, A., Wang, E., Zweig, A., and Ermon, S. Stochastic optimization of sorting networks via continuous relaxations. In *International Conference on Learning Representations*, 2019. URL https://openreview.net/forum?id=H1eSS3CcKX.

Ho, J. and Salimans, T. Classifier-free diffusion guidance, 2022. URL https://arxiv.org/abs/2207.12598.

Ho, J., Jain, A., and Abbeel, P. Denoising diffusion probabilistic models. In *Proceedings of the 34th International Conference on Neural Information Processing Systems*, NIPS '20, Red Hook, NY, USA, 2020. Curran Associates Inc. ISBN 9781713829546.

Jang, E., Gu, S., and Poole, B. Categorical reparameterization with gumbel-softmax. In *International Conference on Learning Representations*, 2017. URL https://openreview.net/forum?id=rkE3y85ee.

Karras, T., Aittala, M., Laine, S., and Aila, T. Elucidating the design space of diffusion-based generative models. In *Proceedings of the 36th International Conference on Neural Information Processing Systems*, NIPS '22, Red Hook, NY, USA, 2022. Curran Associates Inc. ISBN 9781713871088.

Kim, M., Gao, S., Hsu, Y.-C., Shen, Y., and Jin, H. Token fusion: Bridging the gap between token pruning and token merging. In *2024 IEEE/CVF Winter Conference on*

Applications of Computer Vision (WACV), pp. 1372–1381, 2024. doi: 10.1109/WACV57701.2024.00141.

Kingma, D. P. and Ba, J. Adam: A method for stochastic optimization. In Bengio, Y. and LeCun, Y. (eds.), *3rd International Conference on Learning Representations, ICLR 2015, San Diego, CA, USA, May 7-9, 2015, Conference Track Proceedings*, 2015.

Lee, S.-H., Wang, J., Zhang, Z., Fan, D., and Li, X. Video token merging for long-form video understanding. In *Proceedings of the 38th International Conference on Neural Information Processing Systems*, NIPS '24, Red Hook, NY, USA, 2024. Curran Associates Inc. ISBN 9798331314385.

Li, D., Kamko, A., Akhgari, E., Sabet, A., Xu, L., and Doshi, S. Playground v2.5: Three insights towards enhancing aesthetic quality in text-to-image generation, 2024. URL https://arxiv.org/abs/2402.17245.

Lipman, Y., Chen, R. T. Q., Ben-Hamu, H., Nickel, M., and Le, M. Flow matching for generative modeling. In *The Eleventh International Conference on Learning Representations*, 2023. URL https://openreview.net/forum?id=PqvMRDCJT9t.

Liu, S.-Y., Wang, C.-Y., Yin, H., Molchanov, P., Wang, Y.-C. F., Cheng, K.-T., and Chen, M.-H. Dora: weight-decomposed low-rank adaptation. In *Proceedings of the 41st International Conference on Machine Learning*, ICML'24. JMLR.org, 2024.

Loshchilov, I. and Hutter, F. Decoupled weight decay regularization. In *International Conference on Learning Representations*, 2019. URL https://openreview.net/forum?id=Bkg6RiCqY7.

Lu, C., Zhou, Y., Bao, F., Chen, J., Li, C., and Zhu, J. Dpm-solver: a fast ode solver for diffusion probabilistic model sampling in around 10 steps. In *Proceedings of the 36th International Conference on Neural Information Processing Systems*, NIPS '22, Red Hook, NY, USA, 2022. Curran Associates Inc. ISBN 9781713871088.

Lu, W., Zheng, S., Xia, Y., and Wang, S. ToMA: Token merge with attention for diffusion models. In *Forty-second International Conference on Machine Learning*, 2025. URL https://openreview.net/forum?id=51l8tvuIxo.

Mangrulkar, S., Gugger, S., Debut, L., Belkada, Y., Paul, S., Bossan, B., and Tietz, M. PEFT: State-of-the-art parameter-efficient fine-tuning methods. https://github.com/huggingface/peft, 2022.

Marin, D., Chang, J.-H. R., Ranjan, A., Prabhu, A., Rastegari, M., and Tuzel, O. Token pooling in vision transformers for image classification. In *2023 IEEE/CVF Winter Conference on Applications of Computer Vision (WACV)*, pp. 12–21, 2023. doi: 10.1109/WACV56688.2023.00010.

Peebles, W. and Xie, S. Scalable diffusion models with transformers. In *2023 IEEE/CVF International Conference on Computer Vision (ICCV)*, pp. 4172–4182, 2023. doi: 10.1109/ICCV51070.2023.00387.

Perez, E., Strub, F., de Vries, H., Dumoulin, V., and Courville, A. Film: visual reasoning with a general conditioning layer. In *Proceedings of the Thirty-Second AAAI Conference on Artificial Intelligence and Thirtieth Innovative Applications of Artificial Intelligence Conference and Eighth AAAI Symposium on Educational Advances in Artificial Intelligence*, AAAI'18/IAAI'18/EAAI'18. AAAI Press, 2018. ISBN 978-1-57735-800-8.

Podell, D., English, Z., Lacey, K., Blattmann, A., Dockhorn, T., Müller, J., Penna, J., and Rombach, R. SDXL: Improving latent diffusion models for high-resolution image synthesis. In *The Twelfth International Conference on Learning Representations*, 2024. URL https://openreview.net/forum?id=di52zR8xgf.

Rao, Y., Zhao, W., Liu, B., Lu, J., Zhou, J., and Hsieh, C.-J. Dynamicvit: Efficient vision transformers with dynamic token sparsification. In *Advances in Neural Information Processing Systems (NeurIPS)*, 2021.

Robbins, H. and Monro, S. A stochastic approximation method. *The Annals of Mathematical Statistics*, 22(3): 400–407, 1951. ISSN 00034851.

Rombach, R., Blattmann, A., Lorenz, D., Esser, P., and Ommer, B. High-resolution image synthesis with latent diffusion models. In *Proceedings of the IEEE/CVF Conference on Computer Vision and Pattern Recognition (CVPR)*, pp. 10684–10695, June 2022.

Ronneberger, O., Fischer, P., and Brox, T. U-net: Convolutional networks for biomedical image segmentation. In Navab, N., Hornegger, J., Wells, W. M., and Frangi, A. F. (eds.), *Medical Image Computing and Computer-Assisted Intervention – MICCAI 2015*, pp. 234–241, Cham, 2015. Springer International Publishing. ISBN 978-3-319-24574-4.

Saghatchian, O., Moghadam, A. G., and Nickabadi, A. Cached adaptive token merging: Dynamic token reduction and redundant computation elimination in diffusion model. 2025.

Song, J., Meng, C., and Ermon, S. Denoising diffusion implicit models. In *International Conference on Learning*

Representations, 2021. URL https://openreview.net/forum?id=St1giarCHLP.

Sun, W., Tu, R.-C., Liao, J., Jin, Z., and Tao, D. Asymrnr: Video diffusion transformers acceleration with asymmetric reduction and restoration. In *Forty-second International Conference on Machine Learning*, 2025. URL https://openreview.net/forum?id=5PiZevq9fY.

Vaswani, A., Shazeer, N., Parmar, N., Uszkoreit, J., Jones, L., Gomez, A. N., Kaiser, L., and Polosukhin, I. Attention is all you need. In *Proceedings of the 31st International Conference on Neural Information Processing Systems*, NIPS'17, pp. 6000–6010, Red Hook, NY, USA, 2017. Curran Associates Inc. ISBN 9781510860964.

von Platen, P., Patil, S., Lozhkov, A., Cuenca, P., Lambert, N., Rasul, K., Davaadorj, M., Nair, D., Paul, S., Berman, W., Xu, Y., Liu, S., and Wolf, T. Diffusers: State-of-the-art diffusion models. https://github.com/huggingface/diffusers, 2022.

Wang, H., Dedhia, B., and Jha, N. K. Zero-tprune: Zero-shot token pruning through leveraging of the attention graph in pre-trained transformers. In *2024 IEEE/CVF Conference on Computer Vision and Pattern Recognition (CVPR)*, pp. 16070–16079, 2024a. doi: 10.1109/CVPR52733.2024.01521.

Wang, H., Liu, D., Kang, Y., Li, Y., Lin, Z., Jha, N. K., and Liu, Y. Attention-driven training-free efficiency enhancement of diffusion models. In *2024 IEEE/CVF Conference on Computer Vision and Pattern Recognition (CVPR)*, pp. 16080–16089, 2024b. doi: 10.1109/CVPR52733.2024.01522.

Wu, H., Xu, J., Le, H., and Samaras, D. Importance-based token merging for efficient image and video generation, 2025. URL https://arxiv.org/abs/2411.16720.

Yang, X., Yang, Y., Pang, H., Tian, A. X., and Li, L. Freqts: frequency-aware token selection for accelerating diffusion models. In *Proceedings of the Thirty-Ninth AAAI Conference on Artificial Intelligence and Thirty-Seventh Conference on Innovative Applications of Artificial Intelligence and Fifteenth Symposium on Educational Advances in Artificial Intelligence*, AAAI'25/IAAI'25/EAAI'25. AAAI Press, 2025. ISBN 978-1-57735-897-8. doi: 10.1609/aaai.v39i9.33008. URL https://doi.org/10.1609/aaai.v39i9.33008.

You, H., Barnes, C., Zhou, Y., Kang, Y., Du, Z., Zhou, W., Zhang, L., Nitzan, Y., Liu, X., Lin, Z., Shechtman, E., Amirghodsi, S., and Lin, Y. C. Layer- and

timestep-adaptive differentiable token compression ratios for efficient diffusion transformers. In *IEEE/CVF Conference on Computer Vision and Pattern Recognition, CVPR 2025, Nashville, TN, USA, June 11-15, 2025*, pp. 18072–18082. Computer Vision Foundation / IEEE, 2025. doi: 10.1109/CVPR52734.2025.01684.

Yuan, Z., Zhang, H., Pu, L., Ning, X., Zhang, L., Zhao, T., Yan, S., Dai, G., and Wang, Y. DiTFastattn: Attention compression for diffusion transformer models. In *The Thirty-eighth Annual Conference on Neural Information Processing Systems*, 2024. URL https://openreview.net/forum?id=51HQpkQy3t.

Zhang, E., Xiao, B., Tang, J., Ma, Q., Zou, C., Ning, X., Hu, X., and Zhang, L. Token pruning for caching better: 9 times acceleration on stable diffusion for free, 2024a. URL https://arxiv.org/abs/2501.00375.

Zhang, Y., Wei, L., and Freris, N. Synergistic patch pruning for vision transformer: Unifying intra- & inter-layer patch importance. In *The Twelfth International Conference on Learning Representations*, 2024b. URL https://openreview.net/forum?id=COO51g41Q4.

Zhao, W., Han, Y., Tang, J., Wang, K., Song, Y., Huang, G., Wang, F., and You, Y. Dynamic diffusion transformer. In *The Thirteenth International Conference on Learning Representations*, 2025. URL https://openreview.net/forum?id=taHwqSrbrb.

Zou, C., Liu, X., Liu, T., Huang, S., and Zhang, L. Accelerating diffusion transformers with token-wise feature caching. In *The Thirteenth International Conference on Learning Representations*, 2025. URL https://openreview.net/forum?id=yYZbZGo4ei.

A. Theoretical Derivations and Synthetic Validation

In this appendix, we provide formal derivations for the gradient estimators and validate the core mechanisms through synthetic experiments. We detail the Jacobian of the soft ranking operation (Sec. A.1), the formulation of the residual-based gradient estimator (Sec. A.2), and empirical validation on synthetic tasks (Sec. A.3).

A.1. Jacobian and Consistency of the Soft Ranking Matrix

The differentiability of our method hinges on the continuous mapping from scores to ranks. Here, we derive the Jacobian of the soft ranking operation to elucidate how gradients propagate through the sorting mechanism.

Recall that the *descending soft rank* $\tilde{r}_i$ of token i is defined based on pairwise comparisons with all other tokens j:

$$\tilde{r}_i(\mathbf{s}) = 1 + \sum_{j \neq i} \sigma(D_{ji}), \quad \text{where } D_{ji} = \frac{s_j - s_i}{\tau_{\text{rank}}}. \tag{16}$$

In this descending formulation, $D_{ji} > 0$ implies $s_j > s_i$, contributing to a larger (worse) rank index for token i. Let $\pi_i = \sigma((k - \tilde{r}_i)/\tau_{\text{sel}})$ be the selection probability. To update the router scores $\mathbf{s}$, we must compute the gradient of the rank vector $\tilde{\mathbf{r}}$ with respect to the score vector $\mathbf{s}$.

Let $\sigma'(z) = \sigma(z)(1 - \sigma(z))$ denote the derivative of the sigmoid function. We define the pairwise gradient scalar as $\delta_{ji} \triangleq \sigma'(D_{ji})$. The partial derivative of the rank $\tilde{r}_i$ with respect to an arbitrary score s_m is:

$$\frac{\partial \tilde{r}_i}{\partial s_m} = \sum_{j \neq i} \frac{\partial \sigma(D_{ji})}{\partial s_m} = \frac{1}{\tau_{\text{rank}}} \sum_{j \neq i} \delta_{ji} \cdot \frac{\partial(s_j - s_i)}{\partial s_m}. \tag{17}$$

We analyze the two distinct cases for the index m:

Case 1: Self-Sensitivity ($m = i$). We consider the gradient of a token's rank with respect to its own score. In the summation over j, s_i appears in every term as $-s_i$:

$$\frac{\partial \tilde{r}_i}{\partial s_i} = \frac{1}{\tau_{\text{rank}}} \sum_{j \neq i} \delta_{ji} \cdot (-1) = -\frac{1}{\tau_{\text{rank}}} \sum_{j \neq i} \sigma'\left(\frac{s_j - s_i}{\tau_{\text{rank}}}\right). \tag{18}$$

Since $\sigma' > 0$, this diagonal term of the Jacobian is strictly negative. This mathematically confirms that increasing a token's score s_i consistently decreases (improves) its rank index $\tilde{r}_i$.

Case 2: Cross-Sensitivity ($m \neq i$). We consider the gradient of token i's rank with respect to another token m's score. The summation over j vanishes for all terms except where $j = m$:

$$\frac{\partial \tilde{r}_i}{\partial s_m} = \frac{1}{\tau_{\text{rank}}} \cdot \delta_{mi} \cdot (1) = \frac{1}{\tau_{\text{rank}}} \sigma'\left(\frac{s_m - s_i}{\tau_{\text{rank}}}\right). \tag{19}$$

This off-diagonal term is strictly positive, indicating that increasing the score of a competitor token m increases (worsens) the rank of token i.

Global Gradient Flow. By combining these terms via the chain rule, the gradient of the loss $\mathcal{L}$ with respect to a specific score s_m aggregates feedback from the entire sequence:

$$\frac{\partial \mathcal{L}}{\partial s_m} = \sum_{i=1}^{N} \frac{\partial \mathcal{L}}{\partial \pi_i} \cdot \underbrace{\frac{\partial \pi_i}{\partial \tilde{r}_i}}_{\text{Selection}} \cdot \underbrace{\frac{\partial \tilde{r}_i}{\partial s_m}}_{\text{Ranking}}. \tag{20}$$

This formulation highlights the *context-aware* nature of our gradient estimation: updating s_m not only affects the probability of token m being selected (via $\frac{\partial \tilde{r}_m}{\partial s_m}$) but also impacts the selection probabilities of all other tokens i (via $\frac{\partial \tilde{r}_i}{\partial s_m}$), thereby encouraging the router to learn a global sorting policy rather than independent scoring.

A.2. Derivation of the Residual-Based Gradient Estimator

To enable end-to-end optimization of the router parameters despite the discrete hard selection, we employ a Straight-Through Estimator (STE) based on a differentiable surrogate graph.

Surrogate Input-Gating Model. We define the surrogate effective inputs for the selected path ($\mathbf{x}_i^{\text{sel}}$) and the rejected path ($\mathbf{x}_i^{\text{rej}}$) as functions of the inclusion score π_i. This models π_i as a continuous gate modulating the input flow:

$$
\begin{aligned}
\mathbf{x}_i^{\text{sel}} &= \pi_i \cdot \mathbf{x}_i, \\
\mathbf{x}_i^{\text{rej}} &= (1 - \pi_i) \cdot \mathbf{x}_i.
\end{aligned}
\tag{21}
$$

Gradient Derivation. We derive the gradient of the loss $\mathcal{L}$ with respect to π_i via the chain rule. By differentiating Eq. 21, we observe that $\frac{\partial \mathbf{x}_i^{\text{sel}}}{\partial \pi_i} = \mathbf{x}_i$ and $\frac{\partial \mathbf{x}_i^{\text{rej}}}{\partial \pi_i} = -\mathbf{x}_i$. Let ∇^{sel} and ∇^{rej} denote the backpropagated gradients $\frac{\partial \mathcal{L}}{\partial \mathbf{x}^{\text{sel}}}$ and $\frac{\partial \mathcal{L}}{\partial \mathbf{x}^{\text{rej}}}$, respectively. The exact gradient for the surrogate model is derived as:

$$
\begin{aligned}
\frac{\partial \mathcal{L}}{\partial \pi_i} &= \left\langle \frac{\partial \mathcal{L}}{\partial \mathbf{x}_i^{\text{sel}}}, \frac{\partial \mathbf{x}_i^{\text{sel}}}{\partial \pi_i} \right\rangle + \left\langle \frac{\partial \mathcal{L}}{\partial \mathbf{x}_i^{\text{rej}}}, \frac{\partial \mathbf{x}_i^{\text{rej}}}{\partial \pi_i} \right\rangle \\
&= \left\langle \nabla_{\mathbf{x}_i}^{\text{sel}} \mathcal{L}, \ \mathbf{x}_i \right\rangle + \left\langle \nabla_{\mathbf{x}_i}^{\text{rej}} \mathcal{L}, \ -\mathbf{x}_i \right\rangle \\
&= \left\langle \nabla_{\mathbf{x}_i}^{\text{sel}} \mathcal{L} - \nabla_{\mathbf{x}_i}^{\text{rej}} \mathcal{L}, \ \mathbf{x}_i \right\rangle.
\end{aligned}
\tag{22}
$$

Stochastic Single-Path Estimator. In the actual training computation, the deterministic top-k selection activates only one path per token (either $\mathbf{x}^{\text{sel}}$ or $\mathbf{x}^{\text{rej}}$). Consequently, the simultaneous evaluation of both gradient terms in Eq. 22 is impossible. To address this, we construct a stochastic estimator $\hat{g}_i$ that utilizes only the gradient from the executed path:

$$
\hat{g}_i = \frac{\partial \mathcal{L}}{\partial \pi_i} \approx \begin{cases} \left\langle \nabla_{\mathbf{x}_i}^{\text{sel}} \mathcal{L}, \ \mathbf{x}_i \right\rangle & \text{if } i \in \mathcal{I}_{\text{topk}} \\ -\left\langle \nabla_{\mathbf{x}_i}^{\text{rej}} \mathcal{L}, \ \mathbf{x}_i \right\rangle & \text{if } i \notin \mathcal{I}_{\text{topk}} \end{cases}
\tag{23}
$$

The validity of this single-sample estimator relies on the stochastic nature of our training protocol. Specifically, we incorporate *stratified ratio sampling* (varying k dynamically) and *score perturbation* (injecting Gaussian noise ϵ) to prevent tokens from locking into a fixed state. These mechanisms ensure that over the course of training, a token visits both selected and rejected states, allowing the estimator to approximate the expected gradient direction via Monte Carlo sampling.

Gradient Flow to the Budget k. A key advantage of our differentiable sorting formulation is the explicit gradient flow to the learnable budget k. Applying the chain rule, the gradient for k aggregates the sensitivities of all tokens:

$$
\frac{\partial \mathcal{L}}{\partial k} = \sum_{i=1}^{N} \frac{\partial \mathcal{L}}{\partial \pi_i} \cdot \frac{\partial \pi_i}{\partial k}.
\tag{24}
$$

Since π_i is a sigmoid function of k (Eq. 6), the term $\frac{\partial \pi_i}{\partial k}$ is strictly positive. Consequently, the update direction for k is determined by the sum of $\frac{\partial \mathcal{L}}{\partial \pi_i}$. Intuitively, if the aggregate marginal gain of selecting tokens (positive $\hat{g}_i$) outweighs the penalty of rejecting them, the gradient $\nabla_k \mathcal{L}$ will be positive, driving the model to increase the budget k. This allows the model to dynamically learn the optimal number of active tokens required to minimize the task loss.

Differentiable Cost Control via k-Relaxation. Unlike traditional continuous relaxations (Jang et al., 2017) that primarily focus on the differentiability of individual categorical selections, our formulation explicitly treats the budget k as a learnable parameter embedded within the soft inclusion function $\pi_i(k)$. In standard Straight-Through Estimators (STE) or categorical samplers, the number of selected elements is typically either a fixed hyperparameter or a result of independent thresholding. By contrast, our method enables the model to end-to-end optimize the computational cost by propagating gradients directly to k through the sorting-based relaxation. This mechanism effectively bridges the gap between differentiable sorting and dynamic resource allocation, allowing the model to autonomously seek an optimal equilibrium between task performance and sparsity penalty during training.

Analysis of Bias and Variance. We analyze the properties of our estimator $\hat{g}_i$ compared to the ideal surrogate gradient g_i^* (Eq. 22).

- **Bias and Sign Consistency:** While $\hat{g}_i$ is a single-sample approximation, it maintains *sign consistency* with the ideal gradient. If the active path significantly reduces loss (large $\langle \nabla^{\text{sel}}, \mathbf{x} \rangle$), $\hat{g}_i$ is positive, encouraging selection. Conversely, if the residual path induces high error sensitivity (large $\langle \nabla^{\text{rej}}, \mathbf{x} \rangle$), $\hat{g}_i$ becomes negative (due to the sign inversion), penalizing rejection. Thus, the estimator consistently drives the parameters towards the lower-loss path.

- **Variance and Exploration:** The estimator introduces high variance due to the binary nature of the observation. However, in the context of discrete optimization, this variance acts as a regularization term, promoting exploration of the combinatorial search space and preventing premature convergence to suboptimal subsets.

A.3. Validation on Synthetic Data

To empirically validate the theoretical properties of our gradient estimator and the dynamic budgeting mechanism, we conduct controlled experiments on synthetic tasks.

Joint Learning of Scoring and Budgeting. To verify the capability of the Shiva router to simultaneously learn feature-aware ranking and converge to the optimal budget, we constructed a synthetic dataset ($N = 100, D = 16$) comprising 20 high-magnitude signal tokens (mean 10.0) and 80 noise tokens ($k^* = 20$). We initialized the budget at $k = 50$ and employed a dual-optimizer strategy, using Adam (Kingma & Ba, 2015) ($\texttt{lr} = 0.1$) for the router and SGD (Robbins & Monro, 1951) ($\texttt{lr} = 2.0$) for the budget k. The training process consisted of a 100-step warmup followed by a 700-step adaptation phase. As illustrated in Figure 6(a), the router rapidly learns to identify signal tokens during the warmup. Subsequently, the budget k automatically decays and stabilizes around $k \approx 18$. This equilibrium point reflects the optimization trade-off determined by the sparsity penalty weight ($\lambda = 0.1$), where the model retains approximately 95% of the signal tokens while effectively filtering out the noise.

Gradient Consistency. We further investigated the quality of our residual-based gradient estimator by conducting a Monte Carlo simulation with 1,000 independent trials. In each trial, we sampled random input features $\mathbf{X}$ and logits to measure the alignment between our estimated gradients and the ideal feature-aligned direction. Figure 6(b) reveals that the resulting cosine similarity distribution is strictly positive with a mean of 0.825 ± 0.043. This strong alignment confirms that our estimator provides reliable and consistent directional signals for optimization, despite the discrete nature of the selection operation.
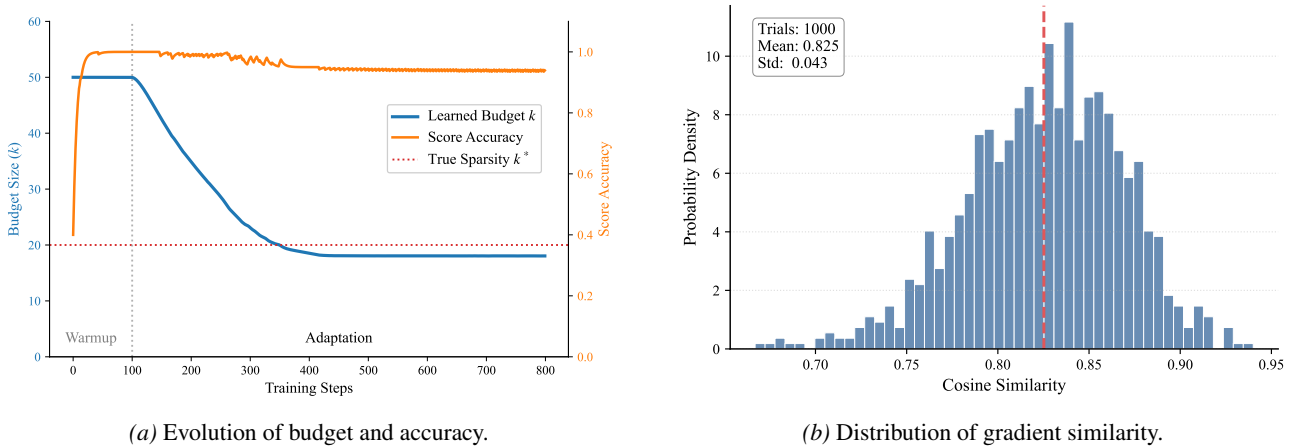

(a) Evolution of budget and accuracy.

(b) Distribution of gradient similarity.

Figure 6. Validation on Synthetic Data. (a) Training dynamics showing the learnable budget k (blue) decaying from 50 and stabilizing near the ground truth sparsity $k^* = 20$ (red dotted line), while the sorting accuracy (orange) remains robust ($\approx 95\%$). (b) Monte Carlo analysis confirms a strong positive alignment (cosine similarity > 0) between our estimated gradients and the ideal optimization direction.

14

A.4. Variance Reduction Analysis of Stratified Sampling

In the main text (Section 3.5), we employ Stratified Timestep Sampling to stabilize the budget estimation. Here, we provide a theoretical justification for why this strategy yields a strictly lower variance estimator compared to standard Uniform Sampling, specifically in the context of diffusion models.

Problem Formulation. Let $r(t) : [0, T] \to [0, 1]$ denote the optimal pruning ratio at timestep t. In diffusion models, $r(t)$ exhibits significant temporal variation across the generation process. Our objective is to estimate the global expected pruning ratio μ over the entire diffusion process: $\mu = \mathbb{E}_{t \sim \mathcal{U}[0,T]}[r(t)]$.

Uniform Sampling Estimator. A standard mini-batch $\mathcal{B}_{uni}$ consists of B independent samples drawn uniformly, i.e., $t_i \sim \mathcal{U}[0, T]$. The Monte Carlo estimator is $\hat{\mu}_{uni} = \frac{1}{B} \sum_{i=1}^{B} r(t_i)$. The variance of this estimator is:

$$\text{Var}(\hat{\mu}_{uni}) = \frac{\sigma^2}{B}, \tag{25}$$

where $\sigma^2 = \text{Var}(r(t))$ represents the total variance of the pruning ratio across the entire timestep domain $[0, T]$.

Stratified Sampling Estimator. We partition the domain $[0, T]$ into B disjoint strata intervals $S_1, \ldots, S_B$, each of length T/B. We draw exactly one sample t_j uniformly from each stratum j. The stratified estimator is $\hat{\mu}_{strat} = \frac{1}{B} \sum_{j=1}^{B} r(t_j)$. According to the *Law of Total Variance*, the total variance σ^2 can be decomposed into the average *within-stratum* variance and the *between-stratum* variance:

$$\sigma^2 = \underbrace{\frac{1}{B} \sum_{j=1}^{B} \sigma_j^2}_{\text{Average Within-Stratum Var}} + \underbrace{\frac{1}{B} \sum_{j=1}^{B} (\mu_j - \mu)^2}_{\text{Between-Stratum Var}}, \tag{26}$$

where σ_j^2 is the variance within stratum j, and μ_j is the expected value within stratum j. Crucially, the variance of the Stratified Estimator is determined only by the within-stratum components:

$$\text{Var}(\hat{\mu}_{strat}) = \frac{1}{B^2} \sum_{j=1}^{B} \sigma_j^2 = \frac{1}{B} \left(\frac{1}{B} \sum_{j=1}^{B} \sigma_j^2 \right). \tag{27}$$

The reduction in variance achieved by Stratified Sampling is explicitly given by the difference between the two estimators:

$$\Delta \text{Var} = \text{Var}(\hat{\mu}_{uni}) - \text{Var}(\hat{\mu}_{strat}) = \frac{1}{B} \underbrace{\left[\frac{1}{B} \sum_{j=1}^{B} (\mu_j - \mu)^2 \right]}_{\text{Between-Stratum Variance}}. \tag{28}$$

Since the term inside the square brackets is a sum of squares, it is strictly non-negative. In DiTs, the pruning ratio $r(t)$ varies significantly across different timesteps, causing the stratum means μ_j to differ substantially from the global mean μ. This makes the *Between-Stratum Variance* term large. By eliminating this term, Stratified Sampling provides a significantly lower-variance gradient estimate, effectively preventing the learnable budget from oscillating due to sampling noise.

B. More Experimental Results

B.1. Impact of Training Strategy on Ratio Generalization

To validate the robustness of our routing mechanism, we visualize the learned policies and score distributions under different training strategies in Figure 7. A critical requirement for our framework is that the router must function effectively across a wide dynamic range of sparsity ratios, as the subsequent Ratio Policy is designed to predict depth-specific keeping rates (e.g., retaining high ratios for shallow texture layers vs. low ratios for deep semantic layers). A router trained with a fixed ratio (e.g., a constant 0.6) typically overfits to a specific sorting threshold, failing to generalize when the Ratio Policy demands a different sparsity level. As shown in the histograms (Figure 7c vs. d), our Stratified Sampling strategy forces the router to learn a more dispersed and discriminative score distribution. This ensures that the rankings remain robust and meaningful regardless of the varying reduction targets imposed by the Ratio Policy, whereas the fixed baseline produces clustered scores with limited differentiability.
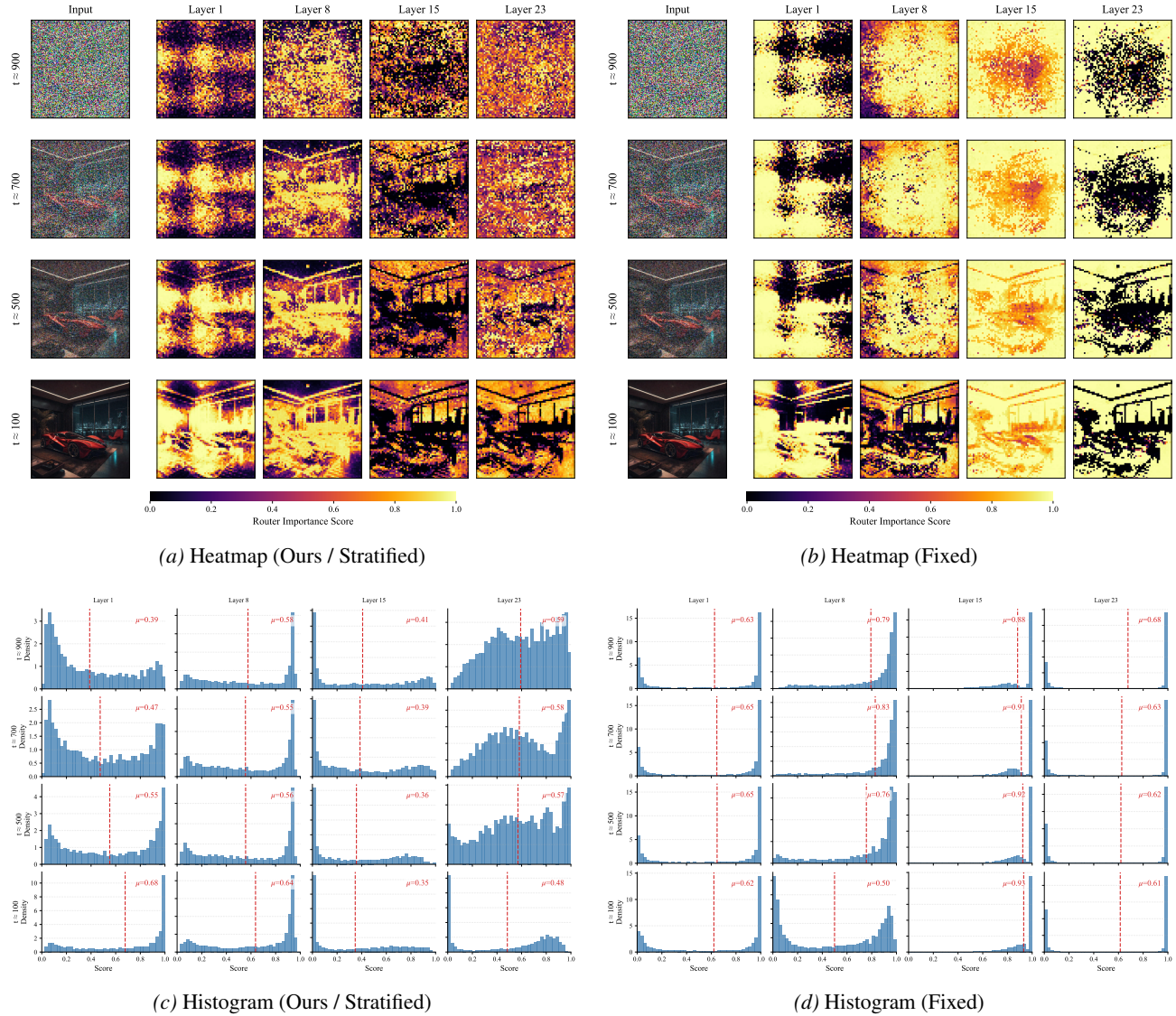

(a) Heatmap (Ours / Stratified)

(b) Heatmap (Fixed)

(c) Histogram (Ours / Stratified)

(d) Histogram (Fixed)

Figure 7. Comparison of Router Training Strategies: Top row (a, b) displays spatial importance heatmaps; Bottom row (c, d) shows the corresponding score distributions. Training with our proposed Stratified Sampling (Left column) exposes the router to varying sparsity levels, resulting in a more dispersed score distribution with a broader dynamic range. This indicates stronger discriminative power between informative and non-informative tokens. In contrast, the Fixed Ratio baseline (Right column) optimizes for a single sorting threshold, leading to a narrow, clustered distribution with limited differentiation.

B.2. Training Details

To ensure the stability of the coupled optimization problem involving the discrete router ranking, the continuous ratio policy, and the generative backbone, we employ a staged training process. This curriculum learning strategy decouples the optimization targets to allow each component to initialize properly before joint optimization.

Stage 1: Router Warmup. In the initial phase, the *Ratio Policy* network is bypassed. To prevent the router from overfitting to a single fixed sparsity level and to encourage it to learn a global ranking capability, we sample the target retention ratio r from a stratified uniform distribution $r \sim \mathcal{U}(r_{\min}, r_{\max})$ as described in Sec. 3.5. The router is forced to adapt to these varying random budgets, thereby learning to discriminate token importance across the entire sparsity spectrum.

Stage 2: Policy Learning. Once the router has converged, we activate the *Ratio Policy* network. In this stage, the training is driven by the *Unbiased Budget Constraint Loss* (Eq.(13)) to align the global expected FLOPs with the target. We employ a global EMA estimator for the budget constraint with a momentum coefficient of $\beta = 0.2$ to ensure stability against batch-wise variance.

Crucially, to prevent the policy from collapsing into a trivial solution (e.g., a flat uniform ratio) due to the strict budget penalty, we introduce a *Logit Noise Injection* mechanism. We add zero-mean Gaussian noise $\epsilon \sim \mathcal{N}(0, 1)$ to the output logits of the policy network before the sigmoid activation:

$$r_{t,l} = \sigma(\text{logit}(r_{t,l}) + \epsilon). \tag{29}$$

This high-variance noise forces the policy to explore the boundaries of the ratio landscape (i.e., testing extreme sparsity or density) during training. Importantly, this noise injection does not compromise convergence. Since the injected noise is zero-mean, the perturbed gradient serves as an unbiased estimator of the true gradient. Optimization algorithms like AdamW (Loshchilov & Hutter, 2019), which rely on moment estimation, effectively filter out the stochastic noise over time, driving the deterministic policy parameters towards the optimal expected logits. The noise merely smooths the optimization landscape to escape local minima without biasing the final solution.

Stage 3: Joint Tuning. In the final stage, the exploration noise is removed. We unfreeze the backbone adaptation parameters, such as LoRA, and jointly fine-tune the Router, Policy, and Backbone. The objective is to minimize the diffusion reconstruction loss while maintaining the established budget constraints. This stage allows the backbone to adapt to the sparse token flow and recover any fine-grained details lost due to pruning.

Hyperparameters and Optimization. All models are trained using the AdamW (Loshchilov & Hutter, 2019) optimizer with mixed-precision (`bfloat16`) to ensure memory efficiency. We utilize a global effective batch size of 16 (micro-batch size 1 per device). The learning rates are set to 3×10^{-4} for the Router and 1×10^{-4} for the Ratio Policy. For $\mu_{\text{global}}^{(k)}$ in Eq.(12), we set β to 0.2. For efficient backbone adaptation, we employ DoRA (Liu et al., 2024) with a rank of $r = 32$, applied to all linear projections within the Attention and FFN blocks. A linear warmup of 200 steps is applied at the beginning of each training stage. To support Classifier-Free Guidance (Ho & Salimans, 2022) (CFG), we randomly drop text captions with a probability of $p = 0.1$. During inference, we use 50 sampling steps with CFG scales of 7.0, 3.5, and 4.5 for SD3.5, Flux, and PixArt, respectively.

Temperature Annealing with Normalized Sorting. In our implementation, we introduce a normalization factor N (sequence length) to Eq. 6 to decouple the gradient scale from the resolution. The modified selection probability is formulated as:

$$\pi_i = \sigma\left(\frac{k - \tilde{r}_i}{\tau_{\text{sel}} \cdot N}\right). \tag{30}$$

To bridge the gap between soft training and hard inference, we employ a deterministic annealing schedule: the ranking temperature τ_{rank} decays from 0.2, and the selection temperature τ_{sel} decays from 0.1, gradually hardening the probability distribution over the course of training.

Normalized Feature Distillation. For intermediate layer distillation, we observed that standard MSE loss is sensitive to the varying feature magnitudes across depths, often necessitating heuristically small loss weights in prior works (Zhao et al.,

2025). To stabilize optimization, we propose *Normalized Feature Distillation*, which applies Layer Normalization before the distance calculation:

$$\mathcal{L}_{\text{distill}} = \sum_l \left\| \text{LayerNorm}(\mathbf{h}_l^{\text{Student}}) - \text{LayerNorm}(\mathbf{h}_l^{\text{Teacher}}) \right\|_2^2. \tag{31}$$

This standardization ensures that the distillation gradient is driven by semantic misalignment rather than numerical scale differences. For comprehensive configuration files, please refer to the attached source code.

B.3. Implementation Details and Baseline Configurations

To ensure reproducibility and facilitate future research, we developed a unified and modular codebase based on the `diffusers` library (von Platen et al., 2022). Below we detail the engineering framework, model-specific adaptations, and baseline configurations.

Adaptive Ratio Policy Network. The policy network employs a decoupled additive architecture comprising two parallel branches. The *Layer Branch* maps the layer index to a hidden embedding ($\mathbb{R}^{256}$) via a learnable lookup table, followed by a 2-layer MLP (Linear→SiLU→Linear) to predict the spatial logit. Simultaneously, the *Time Branch* processes the sinusoidal timestep embedding through a mirrored MLP structure with a hidden dimension of 256. The final retention ratio $r_{t,l}$ is obtained by summing the logits from both branches with a learnable global bias parameter b_{anchor}. For training stability, b_{anchor} is initialized to the inverse sigmoid of the target initial ratio (e.g., $\sigma^{-1}(0.6)$) to ensure the training starts from a valid operating point.

Unified Hook-Based Framework. We implement a flexible, *plug-and-play* acceleration framework that abstracts the token reduction logic from the backbone definition. Instead of invasively modifying the model source code, we utilize a centralized *Hook Manager* to inject custom operations at critical computation stages of a DiT block, including pre/post-Attention, pre/post-FFN, and block boundaries. This design allows our method (and baselines) to be seamlessly applied to diverse architectures such as Stable Diffusion 3 (Esser et al., 2024) (SD3), PixArt-Σ (Chen et al., 2025), and Flux.1-dev (Black Forest Labs, 2024), without specific adaptation code. Furthermore, this modular infrastructure decouples the pruning policy from the model execution, enabling rapid prototyping and iteration of efficient diffusion algorithms in future work.

Model-Specific Adaptations. We address two critical implementation details regarding positional embeddings and guidance strategies:

- **Rotary Positional Embeddings (RoPE):** Handling spatial information varies by architecture. For models like SD3 and PixArt, where absolute positional embeddings are added to the tokens prior to the transformer blocks, no additional handling is required as the spatial information is carried within the token features. However, for models like Flux which apply RoPE at every attention layer, simply discarding tokens breaks the geometric correspondence. In our implementation, we gather the corresponding cosine and sine components of the RoPE cache based on the selected token indices ($\mathcal{I}_{\text{topk}}$). We note that exploring more sophisticated, topology-aware RoPE selection strategies remains a promising direction for future work.

- **Guidance Consistency Strategy:** During inference with Classifier-Free Guidance (CFG), the batch dimension is typically doubled to process conditional ($\mathbf{c}$) and unconditional ($\varnothing$) inputs simultaneously. Independent scoring for these two batches can lead to index mismatch, where different spatial tokens are retained for the cond/uncond branches, causing severe artifacts during the latents combination step. To resolve this, we enforce a *Unified Scoring Policy*. We compute the logits for both branches but perform selection based on the element-wise maximum score:

$$\mathbf{s}_{\text{unified}} = \max(\mathbf{s}_{\text{cond}}, \mathbf{s}_{\text{uncond}}). \tag{32}$$

This ensures that if a token is salient in *either* context (e.g., an object mentioned in the prompt but present in the empty-prompt background), it is preserved in both branches, guaranteeing alignment for the subsequent arithmetic operations.

Baseline Reproduction and Configuration. To ensure a fair comparison, we integrated all baseline methods into our unified framework. For open-source methods, we strictly followed their official implementations; for others, we reproduced them based on the algorithm details provided in their respective papers. All hyperparameters were kept consistent with

the original literature unless otherwise specified. Crucially, for our method (Shiva-DiT), we implement a *First-Block Skip* strategy: we explicitly bypass the token reduction in the very first DiT block. Empirically, we observed that the initial layer is responsible for establishing the fundamental low-level feature space; pruning at this nascent stage leads to training instability and degrades generation quality. Processing the full sequence in the first block stabilizes the importance scoring for subsequent layers with negligible computational overhead.

B.4. Training Efficiency Verification

To substantiate the claims regarding training efficiency, we conduct a rigorous comparison of computational overhead (throughput and latency) between Shiva-DiT, DiffCR (You et al., 2025), and the Vanilla baseline. All models are trained on the MJHQ-30K dataset using $8\times$ NVIDIA H200 GPUs with a global batch size of 16.

Table 4. Training cost comparison measured on $8\times$ H200 GPUs with SD3.5. Shiva-DiT significantly outperforms DiffCR in training speed, maintaining near-baseline efficiency. DiffCR suffers from high latency due to its dual-pass consistency requirement.

Method	Throughput (it/s) ↑	Time/Iter (ms) ↓	Relative Cost
Vanilla	1.86	538	$1.00\times$
DiffCR (You et al., 2025)	1.13	885	$1.65\times$
Shiva (Ours)	**1.73**	**578**	**$1.07\times$**

As presented in Table 4, DiffCR incurs a severe training penalty ($1.65\times$ cost, $\sim$50 min/epoch). This overhead primarily stems from its ratio mechanism, which necessitates dual forward passes to linearly interpolate between different ratio bins. In contrast, although Shiva-DiT introduces additional parameters for the Context-Aware Router and Adaptive Ratio Policy, it maintains high throughput (1.73 it/s, $\sim$35 min/epoch). The negligible overhead ($\sim$7%) validates that our residual-based single-pass design effectively bypasses the computational bottleneck of prior consistent pruning methods.

B.5. Additional Qualitative Results

We provide additional qualitative comparisons on SD3.5-Medium in Figures 8, 9, and 10. While existing baselines often introduce structural distortions or lose fine-grained textures, our method maintains superior visual fidelity and semantic alignment. Compared to both training-free and training-based approaches, Shiva-DiT preserves the structural integrity and intricate details (e.g., textures and reflections) across diverse and complex prompts, closely matching the quality of the Vanilla and Finetuned upper bounds.

Figure 8. Prompt: *a delicate silver link bracelet with a small red seastar attached to it.*

Figure 9. Prompt: *a ragdoll cat dressed in magnificent court attire, worn a crown, sparkling necklace, seated on a throne, surrounded by plates of sweets, realistic direct sun lighting, ultra detailed, super realistic, digital photography.*

Figure 10. Prompt: *Design a superrealistic digital painting of a French Bulldog in a rainy urban scene, wearing a rain jacket. Use dim and moody lighting with street lights and reflections on the pavement to create the perfect atmosphere. Make the rain jacket bright blue and the background dark blue and grey to contrast. Emphasize the urban environment and the rain with a midshot of the dog walking towards the camera.*

B.6. Results on Additional Models

To validate the architectural generalization of Shiva-DiT, we extend our evaluation to Flux.1-dev(Black Forest Labs, 2024) and PixArt-Σ(Chen et al., 2025), with quantitative results detailed in Table 5. We observe substantial acceleration (1.24×) on the compute-dense Flux backbone. Conversely, gains on the lightweight PixArt-Σ are marginal (1.04×), as the reduced FLOPs do not translate linearly to wall-clock speedup due to GPU under-saturation. Additional qualitative comparisons are presented in Figures 11, 12, 13, 14, 15, 16, and 17.

Table 5. Generalization results on Flux.1-dev and PixArt-Σ (1024×1024, 50 steps, RTX 4090). Note that while Shiva achieves a significant speedup (1.25×) on the compute-dense Flux.1-dev, the acceleration on the lightweight PixArt-Σ is more modest (1.08×). This is primarily due to the compact backbone (0.6B) limiting GPU saturation; even scaling to batch size 8 only marginally improves speedup to 1.11×. Additionally, Shiva adopts a conservative pruning rate (Δ FLOPs $\approx 17\%$) for PixArt to strictly preserve generative quality.

(a) Flux-Dev

Method	Quality				Efficiency			
	FID↓	IR↑	CLIP↑	IQA↑	FLOPs (T)	Latency (ms)	Speedup	Δ FLOPs (%)
Vanilla	14.25	0.93	30.56	0.50	44.63	33691	1.00×	0.0
Finetuned	*9.29*	*0.33*	*29.19*	*0.56*				
Shiva	15.03	0.92	30.29	0.53	33.93	26891	1.25×	24.0

(b) PixArt-Σ

Method	Quality				Efficiency			
	FID↓	IR↑	CLIP↑	IQA↑	FLOPs (T)	Latency (ms)	Speedup	Δ FLOPs (%)
Vanilla	11.08	0.93	31.37	0.46	12.97	5910	1.00×	0.0
Finetuned	*9.63*	*0.97*	*31.32*	*0.48*				
Shiva	11.84	0.72	30.63	0.47	10.74	5471	1.08×	17.2

| Vanilla-Flux | **Shiva-Flux** | Finetuned-Flux | Vanilla-Pixart | **Shiva-Pixart** | Finetuned-Pixart |

Figure 11. Prompt: *Wolf in fantasy forest, moonlight with rain, inked style.*

| Vanilla-Flux | **Shiva-Flux** | Finetuned-Flux | Vanilla-Pixart | **Shiva-Pixart** | Finetuned-Pixart |

Figure 12. Prompt: *Hyperdetailed photography, Mount Fuji behind cherry blossoms overlooking Saiko lake.*
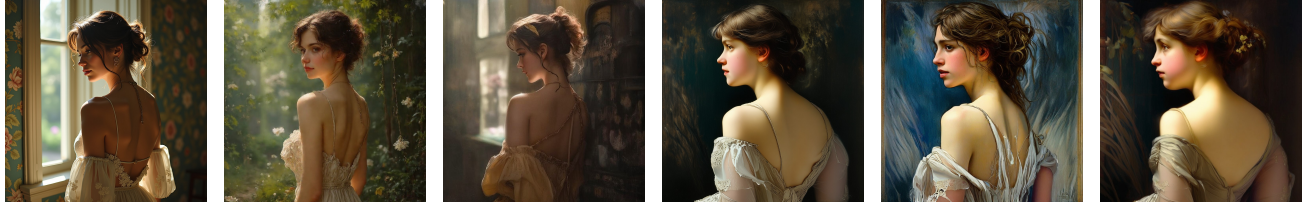
| Vanilla-Flux | **Shiva-Flux** | Finetuned-Flux | Vanilla-Pixart | **Shiva-Pixart** | Finetuned-Pixart |

Figure 13. Prompt: *Young woman in an openback summer dress, looking longingly, visible shoulders, by Henri Gervex, Édouard Manet, JeanHonoré Fragonard, Alfons Mucha, high fantasy, cinematic lighting, romantic atmosphere, ultrarealistic, hyperrealistic, intricate detail.*

| Vanilla-Flux | **Shiva-Flux** | Finetuned-Flux | Vanilla-Pixart | **Shiva-Pixart** | Finetuned-Pixart |

Figure 14. Prompt: *1989 Studio Ghibli anime movie, mythical ocean beach san francisco.*

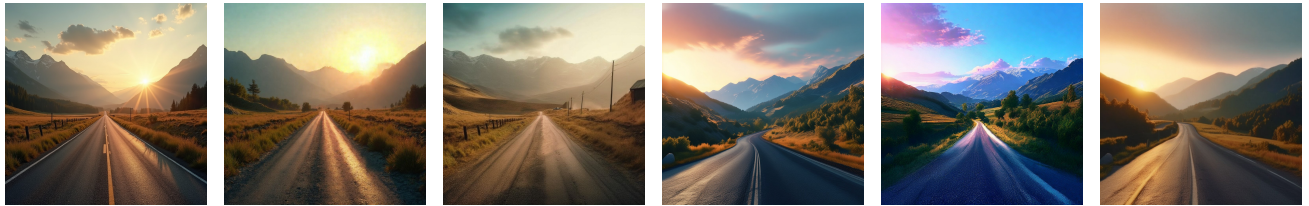| Vanilla-Flux | **Shiva-Flux** | Finetuned-Flux | Vanilla-Pixart | **Shiva-Pixart** | Finetuned-Pixart |

Figure 15. Prompt: *A Fox druid wearing blue colorful robes casting thunder Wave.*
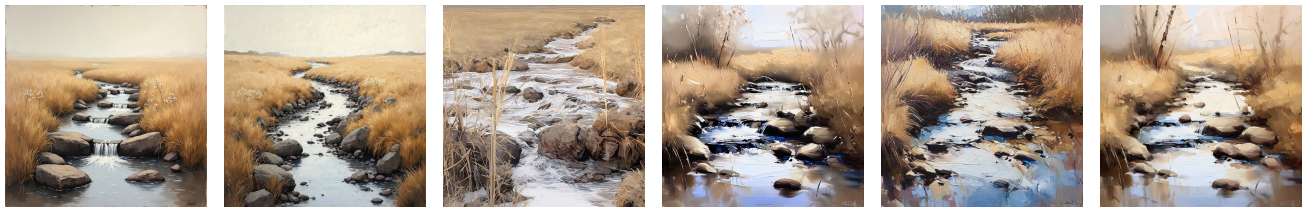

| Vanilla-Flux | **Shiva-Flux** | Finetuned-Flux | Vanilla-Pixart | **Shiva-Pixart** | Finetuned-Pixart |

Figure 16. Prompt: *Country road with mountains in the background at sunrise. realistic footage, ultra details, 4k.*

| Vanilla-Flux | **Shiva-Flux** | Finetuned-Flux | Vanilla-Pixart | **Shiva-Pixart** | Finetuned-Pixart |

Figure 17. Prompt: *Plein air painting, palette knife, loose brushwork, slightly abstract, a thin creek spilling over rocks, drying grass field, soft lighting, soft colors, beige, white, brown, serene, vintage.*